

Article

The AVHRR Polar Pathfinder Climate Data Records

Jeffrey Key ^{1,*}, Xuanji Wang ², Yinghui Liu ², Richard Dworak ² and Aaron Letterly ²

¹ NOAA/NESDIS, 1225 West Dayton St., Madison, WI 53706, USA

² Cooperative Institute for Meteorological Satellite Studies, University of Wisconsin-Madison, 1225 West Dayton St., Madison, WI 53706, USA; xuanjiw@ssec.wisc.edu (X.W.); yinghuil@ssec.wisc.edu (Y.L.); rdworak@ssec.wisc.edu (R.D.); aaron.letterly@ssec.wisc.edu (A.L.)

* Correspondence: jkey@ssec.wisc.edu; Tel.: +1-608-263-2605

Academic Editors: Xuepeng Zhao, Wenze Yang, Viju John, Hui Lu, Ken Knapp, Xiaofeng Li and Prasad S. Thenkabail

Received: 31 December 2015; Accepted: 18 February 2016; Published: 23 February 2016

Abstract: With recent, dramatic changes in Arctic sea ice and the Antarctic ice sheets, the importance of monitoring the climate of the polar regions has never been greater. While many individual global satellite products exist, the AVHRR Polar Pathfinder products provide a comprehensive set of variables that can be used to study trends and interactions within the Arctic and Antarctic climate systems. This paper describes the AVHRR Polar Pathfinder (APP), which is a fundamental climate data record that provides channel reflectances and brightness temperatures, and the AVHRR Polar Pathfinder—Extended (APP-x), which is a thematic climate data record that builds on APP to provide information on surface and cloud properties and radiative fluxes. Both datasets cover the period from 1982 through the present, twice daily, over both polar regions. APP-x has been used in the study of trends in surface properties, cloud cover, and radiative fluxes, interactions between clouds and sea ice, and the role of land surface changes in summer warming.

Keywords: Polar regions; Arctic; Antarctic; climate data record; AVHRR; clouds; radiation; sea ice

1. Introduction

The Arctic has changed dramatically in recent decades and is warming at a greater rate than the rest of the globe. This phenomenon, known as “polar amplification”, is expected to continue over the next century [1–3]. Arctic sea ice extent and thickness have decreased significantly [4–6], in part due to changes in large-scale atmospheric circulation [7,8]. The Arctic is the most highly variable and sensitive part of the global climate system [9,10].

The Antarctic has also been changing, though in distinctly different ways than the Arctic. There has been a major warming of the Antarctic Peninsula over the last 50 years [11], and an associated increase in ice discharge. In contrast, there is some evidence that the Antarctic ice sheet has been gaining ice in the 1990s and 2000s [12]. The uncertainty in these and other polar climate issues is further motivation for developing the APP and APP-x datasets.

Continuous and spatially-robust measurements of the surface and atmospheric properties are therefore important for monitoring and understanding polar climate. Surface-based measurements are essential, as they provide accurate observations of many surface, near-surface, and atmospheric properties, generally at a high temporal sampling rate. They provide measurements of some characteristics that cannot be measured from space, such as surface winds over land and sea ice. However, *in situ* observations do not provide the spatial coverage that can be obtained from space-based instruments. With some satellite data records approaching 40 years in length, we can now examine recent trends and spatial variability in a variety of geophysical variables.

This paper describes two satellite climate data records (CDR) for the polar regions. Both are based on data from the Advanced Very High Resolution Radiometer (AVHRR) onboard the U.S. National Oceanic and Atmospheric Administration (NOAA) polar-orbiting satellites. The AVHRR Polar Pathfinder (APP) is a fundamental climate data record that provides AVHRR channel reflectances and brightness temperatures. The AVHRR Polar Pathfinder-Extended (APP-x) is a thematic climate data record that builds on APP to provide information on surface and cloud properties, as well as radiative fluxes. Both datasets cover the period from 1982 through the present, twice daily, over both polar regions. APP and APP-x were initially developed in the 1990s [13]. They have since been redesigned and enhanced. Here we describe the construction and characteristics of the two datasets. Only a summary is provided; details can be found in the CDR Algorithm Theoretical Basis Documents (C-ATBD) [14,15]. Calibration of APP and validation of APP-x processes is detailed, and examples of how the data have been used to study Arctic and Antarctic climate change are summarized.

2. The AVHRR Polar Pathfinder (APP) Dataset

APP is a fundamental climate data record (FCDR). Its purpose is to provide calibrated and navigated sensor data for the retrieval of higher-level geophysical parameters. In particular, it is the primary input to the extended AVHRR Polar Pathfinder Product, APP-x.

APP is constructed from NOAA AVHRR data. It is comprised of AVHRR channel data (reflectances of visible channels and brightness temperatures of thermal channels), viewing and illumination geometry (sensor scan angle, solar zenith angle, and sun-sensor relative azimuth angle), Universal Coordinated Time (UTC) of the data acquisition, and a surface type mask. The data includes twice-daily composites on a 5 km Equal-Area Scalable Earth (EASE)-Grid over both the Arctic and Antarctic, from 1982 to the present.

The daily APP composites are centered on local solar times (LST) of 04:00 and 14:00 for the Arctic and 02:00 and 14:00 for the Antarctic. While the afternoon time is high sun, it could be nighttime for some polar areas in winter. The purpose of compositing based on local solar time rather than synoptic time (e.g., 0 and 12 UTC everywhere) is to capture the diurnal cycle at all locations. Each composite is composed of as many as 23 orbits from the previous day, the current day, and the next day, depending on the longitude of a pixel. APP covers the north polar region (Arctic) from 48.4 degrees northward, and the south polar region (Antarctic) from -53.2 degrees southward.

2.1. Instruments and Satellites

The AVHRR flies on all NOAA polar-orbiting operational environmental satellites (POES) [16]. The AVHRR instruments onboard TIROS-N, NOAA-6, NOAA-8, and NOAA-10 are designated as AVHRR/1, which has only four spectral channels. The AVHRR onboard NOAA-7, NOAA-9, NOAA-11, and NOAA-14 are designated as AVHRR/2, which has five spectral channels. A version of the AVHRR with six spectral channels, AVHRR/3, is used on NOAA-15 and beyond. Channel 3a, with central wavelength at $1.61 \mu\text{m}$, operates in the daylight part of the orbit while channel 3b operates in the night portion of the orbit. Channel 3a and channel 3b cannot operate simultaneously. The specifications of the AVHRR channels are listed in Table 1.

Table 1. Spectral specifications of AVHRR/1,/2, and /3.

| Channel | TIROS-N | NOAA-6, 8, 10 | NOAA-7, 9, 11, 12, 14 | NOAA-15 and Onward |
|---------|---------------------------|---------------------------|---------------------------|---------------------------|
| | AVHRR/1 | AVHRR/1 | AVHRR/2 | AVHRR/3 |
| 1 | 0.55–0.90 μm | 0.58–0.68 μm | 0.58–0.68 μm | 0.58–0.68 μm |
| 2 | 0.725–1.10 μm | 0.725–1.10 μm | 0.725–1.10 μm | 0.725–1.00 μm |
| 3A | | | | 1.58–1.64 μm |
| 3B | 3.55–3.93 μm | 3.55–3.93 μm | 3.55–3.93 μm | 3.55–3.93 μm |
| 4 | 10.50–11.50 μm | 10.50–11.50 μm | 10.30–11.30 μm | 10.30–11.30 μm |
| 5 | Ch4 repeated | Ch4 repeated | 11.5–12.50 μm | 11.50–12.50 μm |

The instrument scans in the cross-track direction with a field-of-view (FOV) of $\pm 55.37^\circ$ from nadir, and has an instantaneous FOV (IFOV) of 1.1 km at nadir (1.3–1.4 milliradians by 1.3–1.4 milliradians for all channels). The full-resolution AVHRR data are stored and processed in the High Resolution Picture Transmission (HRPT) and Local Area Coverage (LAC) formats. The full-resolution data is also processed onboard the satellite into Global Area Coverage (GAC). To produce GAC data, four out of every five samples along the scan line are used to compute one average value and the data from every third scan line are processed. This yields a 1.1 km by 4 km resolution at the subpoint with a 3.3 km gap between pixels across the scan line at nadir. Generally, the GAC data are considered to have a 4 km resolution. Details of the AVHRR instruments and data can be found in [16].

AVHRR GAC data are used to generate APP. Only the NOAA satellites listed in Table 2 are used in the creation of APP, because these satellites carry AVHRR instruments with all five channels and the equatorial crossing times (ECT) of these satellites are similar. Five-channel AVHRRs are needed for most geophysical parameter retrievals, so the NOAA satellites before NOAA-7 and even-numbered satellites before NOAA-11 are not included. NOAA-16 switches between channel 3A (daytime) and 3B (nighttime), while NOAA-18 has only channel 3B after 5 August 2005. In APP, channels 3A and 3B data are included only for NOAA-16; only channel 3B data are included for other satellites.

Table 2. NOAA POES satellites used in APP.

| NOAA Satellite | Time Range |
|----------------|----------------------------------|
| NOAA-7 | 1 January 1982–31 December 1984 |
| NOAA-9 | 1 January 1985–7 November 1988 |
| NOAA-11 | 8 November 1988–31 December 1994 |
| NOAA-14 | 1 January 1995–31 December 2000 |
| NOAA-16 | 1 January 2001–9 August 2005 |
| NOAA-18 | 10 August 2005–31 December 2009 |
| NOAA-19 | 1 January 2010–present |

Significant variations in the ECT of a satellite will impact the accuracy in generating a consistent time series. There have been considerable drifts in the NOAA POES ECTs, as shown in Figure 1. The APP compositing procedure mitigates this problem to some extent, because each composite is comprised of data mostly within 1–2 hours of the target times.

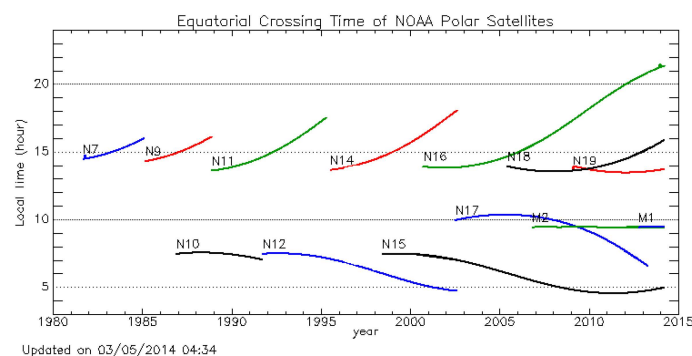


Figure 1. Equatorial crossing time (ECT) of NOAA POES [17].

2.2. Processing Method

The generation of APP daily composites follows the following steps:

- 1 AVHRR GAC Level 1b data from the previous day, the current day, and the next day are acquired. As many as 23 overpasses may be used.
- 2 The data are calibrated to obtain the visible channel reflectances and thermal channel brightness temperatures (BT).

- 3 The data are navigated to obtain accurate longitude/latitude and viewing angles.
- 4 Overpasses within a time window centered on 04:00 and 14:00 local solar time (LST) for the Arctic, and 02:00 and 14:00 LST for the Antarctic, are combined/composited based on sensor scanning angle and time difference from the target time. Only those pixels in the overpasses whose time is within three hours of the target time are considered, and most of data are within 1–2 hours of the target time. A pixel in an overpass updates the composite image pixel if the sensor scan angle for that pixel is less than (closer to nadir) the one that was previously used.

The twice-daily composites that comprise the APP FCDR consist of AVHRR channel reflectances and brightness temperatures, sensor scan angle, solar zenith angle, sun-sensor relative azimuth angle, Universal Coordinated Time (UTC) of the data acquisition, and a surface type mask. The surface type is based on passive microwave data [18].

The AVHRR shortwave channel calibration is determined pre-launch [16]. After launch, the instrument can only be calibrated indirectly, as there is no onboard calibration source for channels 1, 2, and 3A. Calibration of these channels follows the methodology described in [19,20], which is time-dependent and focuses on minimizing inter-satellite differences. This is critical for climate data records, as differences between the satellites can introduce biases in derived trends. Calibration of the AVHRR thermal bands, channels 3b, 4, and 5, is done according to [16] using the onboard blackbody counts and a nonlinear correction.

Examples of APP channels 1 and 2 reflectances and channel 4 brightness temperatures for the Arctic and Antarctic are given in Figure 2. Discontinuities between the orbits that make up the local solar time composites can be seen in some of the images. Comparisons to the NASA MODerate resolution Imaging Spectroradiometer (MODIS) were done by generating a MODIS composite dataset similar in form to APP. Daily MODIS composites were generated at 04:00 and 14:00 LST on a 5 km EASE-Grid resolution using 1 km resolution Aqua MODIS data, including MODIS channel 1 (0.62–0.67 μm), 2 (0.841–0.876 μm), channel 22 (3.929–3.989 μm), 31 (10.78–11.28 μm), and 32 (11.77–12.27 μm).

An example of a comparison between APP and Aqua MODIS composites is shown in Figures 3 and 4. For these cases, the bias, calculated as the mean of all differences over the image composite, and standard deviation between APP and MODIS Aqua channel 1 composites are -0.98% and 10.71% , respectively, for Julian day 182 of 2007, and -1.51% and 13.13% for day 182 of 2003 at 14:00 LST of Arctic. For channel 4 composites, the bias and one standard deviations are 0.12 K and 5.69 K for day 1 of 2007, and 0.32 K and 4.73 K for day 1 of 2003 at 14:00 LST. The small bias in both visible reflectances and infrared brightness temperature is encouraging. The relatively larger standard deviation may be due to the fact that these two composites are at somewhat different wavelengths, times, and viewing angles.

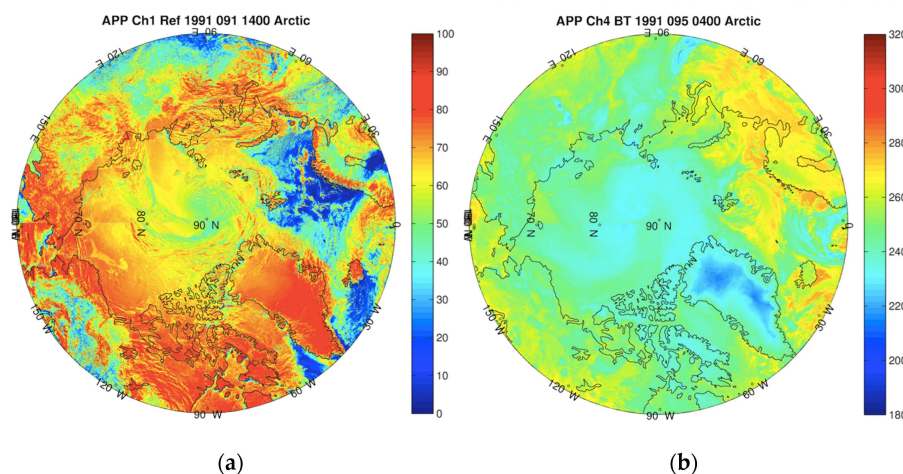


Figure 2. Cont.

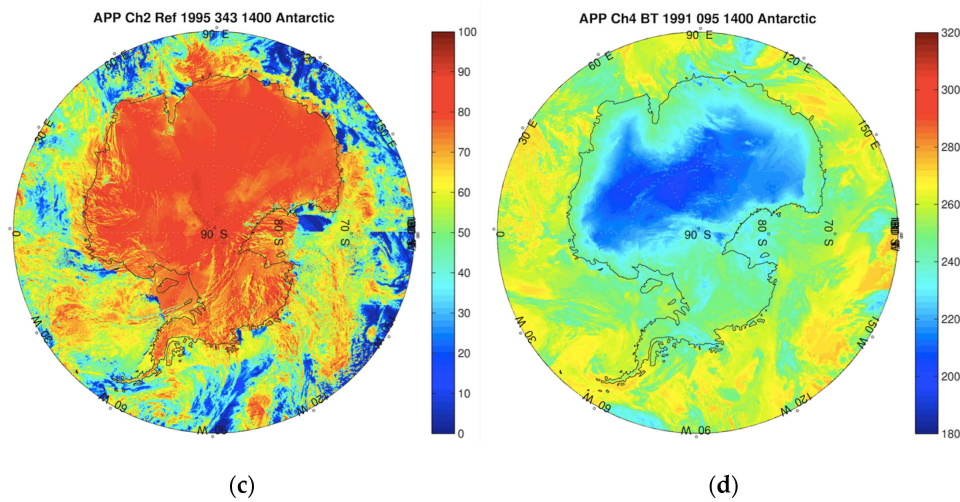


Figure 2. Top: APP channel 1 reflectance (%) over the Arctic on Julian day 91 of 1991 at 14:00 local solar time (LST) (a), and channel 4 brightness temperature (K) on day 95 of 1991 at 04:00 LST (b). Bottom: APP channel 2 reflectance over the Antarctic on day 343 of 1995 at 14:00 LST (c), and channel 4 brightness temperature on day 95 of 1991 at 14:00 LST (d).

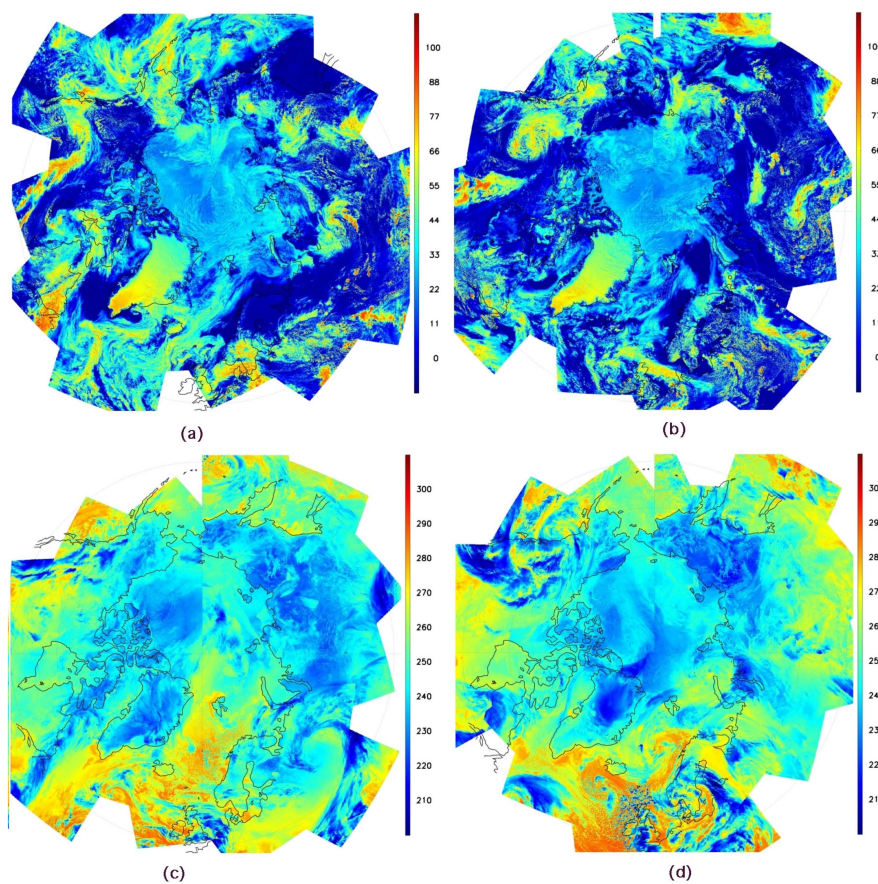


Figure 3. An example of APP processing applied to MODIS data, for comparison to the APP composites in Figure 4. Statistics are given in the text. Top: MODIS 0.64 μm reflectance over the Arctic on day 182 of 2003 (a), and on day 182 of 2007 (b) at 14:00 local solar time (LST). Bottom: MODIS 11 μm brightness temperature on day 1 of 2003 (c), and on day 1 of 2007 (d) at 14:00 LST.

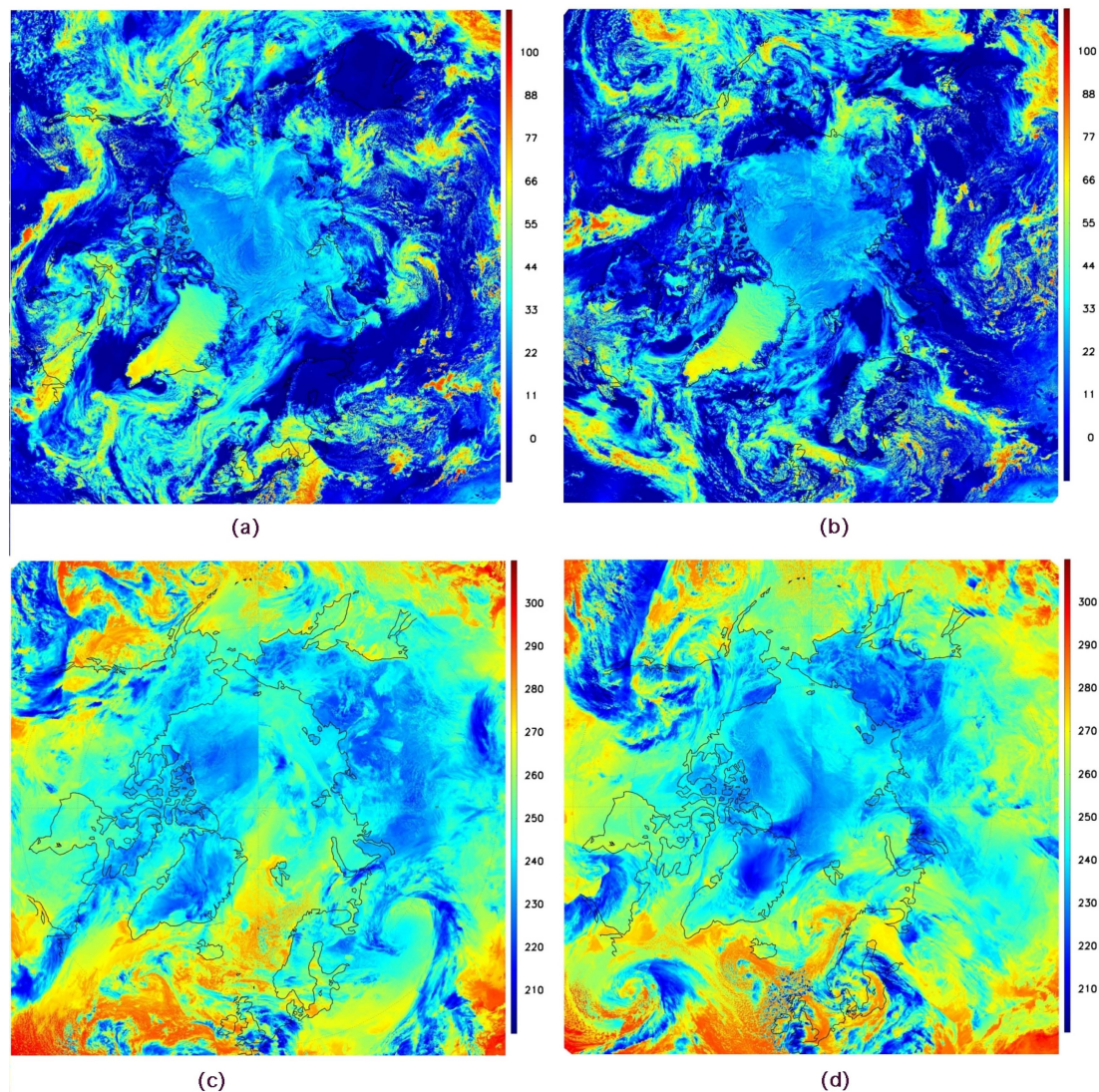


Figure 4. The APP product for the dates and channels corresponding to the MODIS composites in Figure 3. Top: APP channel 1 reflectance over the Arctic on day 182 of 2003 (a), and on day 182 of 2007 (b) at 14:00 local solar time (LST). Bottom: APP channel 4 brightness temperature on day 1 of 2003 (c), and on day 1 of 2007 (d) at 14:00 LST.

3. The AVHRR Polar Pathfinder—Extended (APP-x) Dataset

APP-x contains 19 geophysical variables. All of them have undergone various degrees of validation, though all are not considered CDR quality. The term “CDR quality” is used here in a qualitative sense to indicate that validation results have demonstrated a relatively low uncertainty, such that the variable may be suitable for climate studies. Variables that are difficult to validate due to the lack of *in situ* data are by default not of CDR quality. The APP-x variables are listed below. Those considered to be of CDR quality based on validation studies are identified with an asterisk:

- Surface skin temperature, all-sky, snow, ice, and land*
- Surface broadband albedo, all-sky*
- Sea ice thickness*
- Surface type
- Cloud mask*
- Cloud particle thermodynamic phase
- Cloud optical depth
- Cloud particle effective radius
- Cloud top temperature
- Cloud top pressure
- Cloud type
- Downwelling shortwave radiation at the surface*
- Downwelling longwave radiation at the surface*
- Upwelling shortwave radiation at the surface*
- Upwelling longwave radiation at the surface*
- Upwelling shortwave radiation at the TOA*
- Upwelling longwave radiation at the TOA*
- Shortwave cloud radiative forcing at the surface
- Longwave cloud radiative forcing at the surface

APP-x data are mapped to a 25 km EASE grid at two local solar times: 04:00 and 14:00 for the Arctic, and 02:00 and 14:00 for the Antarctica. APP-x processing starts with the standard APP product and ancillary data. The 25 km APP-x resolution is obtained by subsampling, not averaging, APP. Every fifth APP pixel is selected for APP-x processing. This is done primarily as a matter of computational efficiency but also to preserve the integrity of the radiance data. While averaging would reduce noise, it would result in a loss of information.

APP channel reflectances and brightness temperatures, sensor viewing angle, solar zenith angle, relative azimuth angle, and time are employed in the generation of APP-x. Additionally, some model information is needed: surface air pressure, surface air temperature, surface humidity, surface wind, and atmospheric temperature and humidity profiles. These variables are obtained from the NASA Modern Era Retrospective-analysis for Research and Applications (MERRA) reanalysis [21].

Cloud detection is then performed and the cloud mask feeds into most of the other algorithms. Cloud properties, surface temperature, and surface albedo are then retrieved. Cloud and surface properties are used as input to a parameterized radiative transfer model (a neural network) to calculate radiative fluxes and cloud radiative forcing. Ice thickness is calculated from the One-dimensional Thermodynamic Ice Model (OTIM) using many of the previously-calculated variables as input.

Detailed algorithm descriptions are beyond the scope of this paper. Algorithms are summarized below, first for surface properties then for clouds and radiation. Details are given in the references provided and in [15]. Examples of APP-x are given in Figure 5 for the Arctic and Figure 6 for the Antarctic.

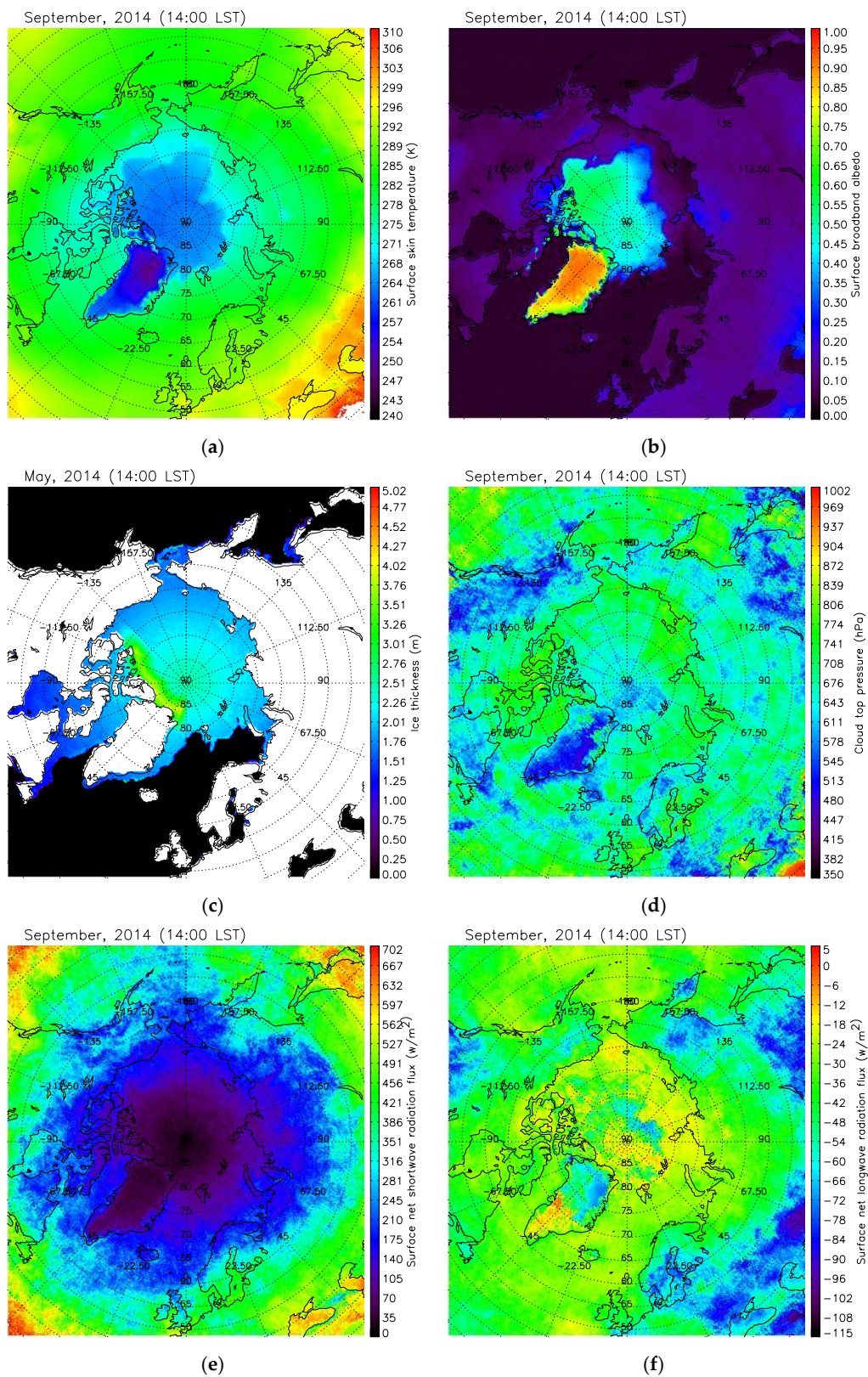


Figure 5. Examples of some APP-x variables over the Arctic. Monthly means are for September 2014 except for sea ice thickness, which is May 2014. Shown are surface skin temperature (a), surface broadband albedo (b), sea ice thickness (c), cloud top pressure (d), surface net shortwave radiative flux (e), and surface net longwave radiative flux (f).

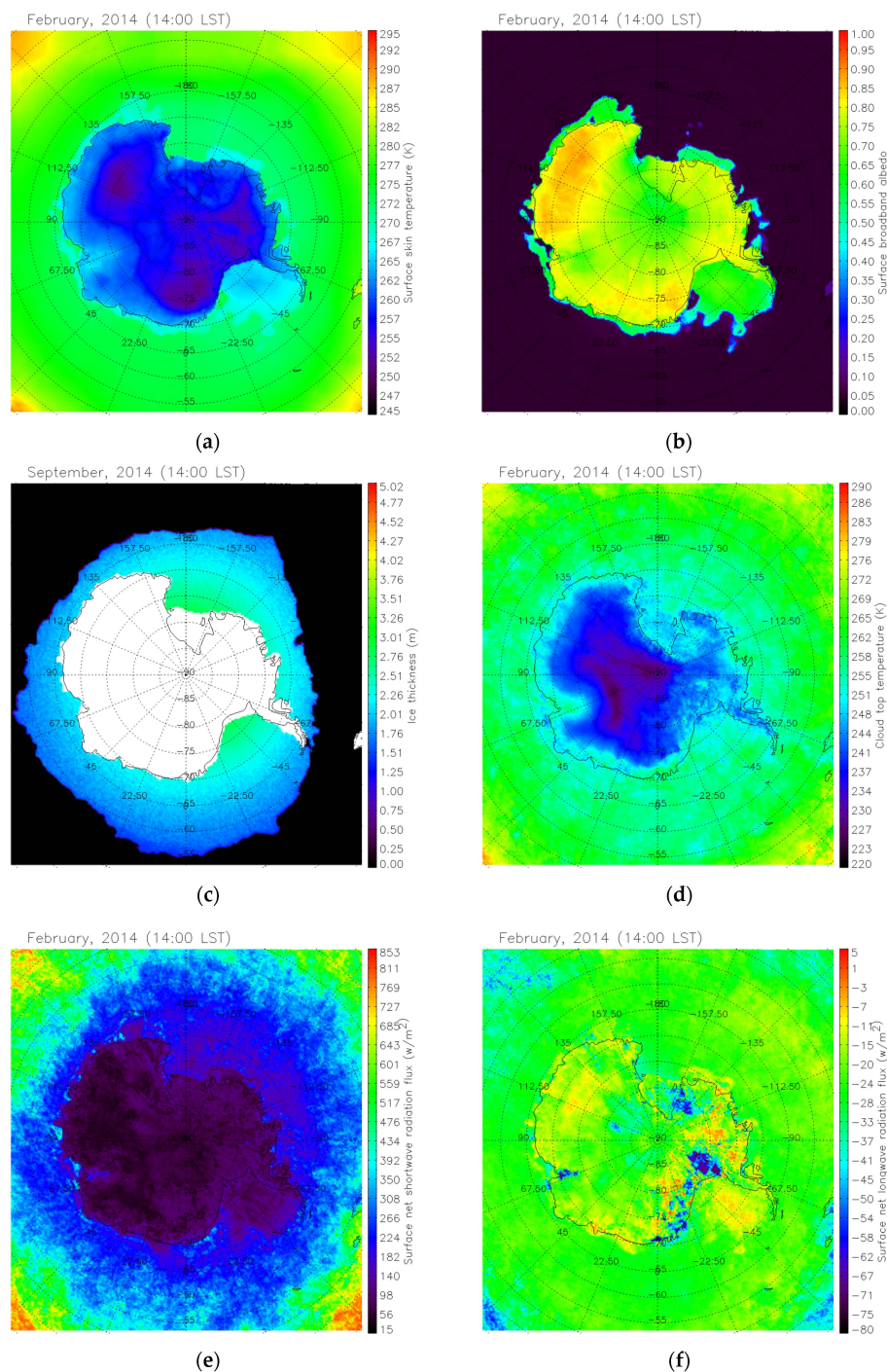


Figure 6. Examples of some APP-x variables over the Antarctic. Monthly means are for February 2014 except for sea ice thickness, which is for September 2014. Shown are surface skin temperature (a), surface broadband albedo (b), sea ice thickness (c), cloud top temperature (d), surface net shortwave radiative flux (e), and surface net longwave radiative flux (f).

3.1. Algorithm Overviews: Surface Properties

For the retrieval of clear-sky surface temperature a simple regression model is used to correct for atmospheric attenuation. To determine the empirical relationship, radiosonde data from drifting ice and land stations in the Arctic and Antarctic were used with a radiative transfer model to simulate the sensor brightness temperatures. The cloudy-sky surface temperature calculation is based on empirical

(linear regression) relationships between the clear sky temperature, wind speed, and solar zenith angle (daytime), determined using surface observations from the SHEBA (Surface HEat Budget of the Arctic) experiment in 1997 north of Alaska. The cloudy-sky estimate applies only to sea ice. The clear-sky surface temperatures are interpolated to cloudy pixels with a kriging function, and then the cloudy sky temperatures are estimated from the clear temperatures, wind speed, and solar zenith angle.

The regression method of relating modeled brightness temperatures to surface temperature is also used for a snow-free land algorithm. Since spectral emissivities for vegetation in channels 4 and 5 are variable and generally unknown, they are variables in the regression. Additionally, scan angle is not a variable in the regression since its dependence on angular emissivity is unknown. The surface temperature retrieval methods for both sea ice/snow and snow-free land are described in [22,23].

The retrieval of surface albedo involves four steps:

1. Convert channels 1 and 2 narrowband reflectances to a broadband reflectance.
2. Correct the top-of-atmosphere (TOA) broadband reflectance for anisotropy.
3. Convert the TOA broadband albedo to a surface broadband albedo.
4. Adjust the surface clear sky broadband albedo for the effects of cloud cover in cloudy pixels (over snow/ice only).

Terminology for albedo varies. Here we distinguish between "inherent" and "apparent" surface albedos. The inherent albedo is the no-atmosphere, or "black-sky", albedo of the surface and is independent of changes in atmospheric conditions. The apparent albedo is what would be measured by up- and down-looking radiometers in the field. It varies with atmospheric conditions. Both vary with solar zenith angle and are directional in that regard. The difference between them is very small for the ocean but can be large for vegetation and snow. APP-x calculates the directional-hemispherical apparent albedo. After the apparent albedo is calculated it is adjusted for cloud cover. The complete procedure is detailed in [24].

The ice thickness retrieval is based on the One-dimensional Thermodynamic Ice Model (OTIM) described in [25]. OTIM estimates ice thickness assuming a surface energy balance at thermo-equilibrium. It employs all components of the surface energy budget to estimate sea and lake ice thickness up to 5 m, though the uncertainty increases for very thick ice. The advantage of this approach is that there is a solid physical foundation. It is capable of retrieving daytime and nighttime sea and lake ice thickness under both clear and cloudy conditions. It is computationally efficient compared to more complex models (e.g., the Community Sea Ice Model). The disadvantage of this approach is that the accuracy of input parameters, including snow depth, surface air humidity, temperature, and wind, can significantly impact the accuracy of ice thickness estimates. The daytime retrieval is sensitive to ice and snow optical properties, which are associated with ice type and thickness, and is therefore less reliable than the nighttime retrieval. Ice thickness is produced for each pixel that is identified as being ice covered. There are no direct AVHRR channel data used by the algorithm. Instead, OTIM relies on other retrieved products from APP-x as well as built-in parameterization schemes for radiative fluxes.

3.2. Algorithm Overviews: Clouds and Radiative Fluxes

The cloud masking procedure used for APP-x consists of thresholding operations that are based on modeled sensor radiances. The AVHRR radiances are simulated for a wide variety of surface and atmospheric conditions with the radiative transfer model Streamer [26], and values that approximately divide clear from cloudy scenes are determined. The single-image cloud mask uses four primary spectral tests: split-window cirrus test, warm cloud test, low stratus-thin cirrus tests, and cold cloud-surface temperature tests. Most were developed and/or used elsewhere but refined and extended over the last two decades [27] for use in APP-x. The application of the spectral tests is conceptually simple: initialize the cloud mask to clear then apply the spectral cloud tests to label cloudy pixels. Two additional tests are used to "restore" cloudy pixels to clear where necessary.

Since spectral tests alone often fail to properly identify cloud cover, particularly with the limited spectral information available from the AVHRR, changes in spectral characteristics over time are also examined. The time series cloud masking procedure operates on a sequence of images acquired on consecutive days at approximately the same solar time. It first applies spectral tests for an initial labeling of cloudy and clear pixels then further refines the identification of clear pixels by examining changes in spectral characteristics from one day to the next. The clear pixels that result from these spectral and temporal tests are used to construct clear-sky radiance statistics over a five-day period for various spectral channels. The statistics are then used in a final thresholding operation to label/relabel pixels as either clear or cloudy.

In APP-x, all clouds are composed of either liquid droplets ("water cloud") or solid ice crystals ("ice cloud"). No attempt is made to identify mixed-phase or multilayer clouds, though we acknowledge that they are common in the polar regions. The theoretical background for these procedures is detailed in [28].

The importance of cloud optical depth and the particle effective radius for remote sensing lies in the fact that the optical properties of clouds used in the calculation of radiative fluxes—the single scattering albedo, the asymmetry parameter, and the extinction coefficient—are proportional to the optical depth and effective radius. Cloud optical depth (unitless) is a measure of the cumulative depletion of radiation as it passes through the cloud. Cloud optical depth retrievals are done using a comprehensive database of modeled reflectances and brightness temperatures covering a wide range of surface and atmospheric conditions. The basic approach for daytime retrievals of water (liquid) cloud follows that of Nakajima and King [29], with simulations of reflectances and brightness temperatures done specifically for a snow/ice surface and high-latitude conditions.

The cloud temperature is determined from the channel 4 brightness temperature, the clear sky brightness temperature (not corrected for the atmosphere), and the visible cloud optical depth. The infrared optical depth is determined from the visible optical depth using parameterizations of cloud optical properties. If the cloud optical depth is less than some threshold, the brightness temperature is assumed to be a function of both the cloud temperature and the upwelling radiation from the surface and atmosphere below the cloud. For opaque clouds the cloud top temperature is simply the channel 4 temperature. If the cloud is not opaque, then the cloud temperature is determined by first computing the cloud transmittance then calculating the cloud radiance that would be required to produce the observed radiance of the cloudy pixel, given the cloud optical thickness and the observed clear sky radiance.

Upwelling and downwelling shortwave and longwave fluxes at the surface and top-of-atmosphere (TOA) are computed with a neural network trained to simulate a radiative model. This is for computational efficiency, as running a radiative transfer model on every pixel would be prohibitive. The neural network, called FluxNet, was trained with Streamer [26]. FluxNet is up to 10,000 times faster than Streamer, and is nearly as accurate.

The cloud radiative effect, more commonly called "cloud forcing", is computed from the net shortwave and longwave fluxes at the surface and TOA. It is defined as:

$$CF_{\lambda} = \int_0^{A_c} \frac{\partial F_{\lambda}}{\partial a} da = F_{\lambda}(A_c) - F_{\lambda}(0) \quad (1)$$

where F_{λ} is the net flux (W m^{-2}) for shortwave or longwave radiation (λ) at the surface and A_c is the cloud fraction in the scene. The net flux is equal to the downwelling minus the upwelling fluxes. Since pixels are assumed to be either completely cloudy or completely clear, the right side of the equation is simply the net flux (shortwave or longwave) for a cloudy pixel minus the net flux if the pixel were clear. Analogous to net radiation, the all-wave net cloud forcing at the surface can be calculated from:

$$CF = CF_{\text{shortwave}} + CF_{\text{longwave}} \quad (2)$$

3.3. Validation

Most of the APP-x parameters were compared with field campaign and meteorological station measurements. Errors and uncertainties are summarized in Table 3. Surface temperature, albedo, cloud fraction, and radiative fluxes were validated against *in situ* measurements at the SHEBA ship. Satellite-derived quantities were calculated for 5 km pixels and averaged over a 25 × 25 km² area centered on the ship. Ice thickness validation was done with data from the NASA IceBridge aircraft campaign. The bias is the difference between satellite-derived quantities and *in situ* measurements. The root-mean-square error (RMSE) is the square root of the mean squared difference between the satellite and *in situ* quantities.

Table 3. Biases and uncertainties (root-mean-square error, RMSE) for some APP-x variables.

| Quantity | Bias | RMSE |
|---|----------------------|-----------------------|
| Surface temperature | 0.20 K | 1.98 K |
| Surface broadband albedo | −0.05(absolute) | 0.10 |
| Ice thickness | −0.22 m | 0.63 m |
| Cloud fraction | 0.14 (absolute) | 0.26 |
| Cloud Particle Phase | 95% correct typing | |
| Downwelling shortwave radiation flux at the surface | 9.8 W/m ² | 34.4 W/m ² |
| Downwelling longwave radiation flux at the surface | 2.1 W/m ² | 22.4 W/m ² |
| Upwelling shortwave radiation flux at the surface | 4.4 W/m ² | 26.6 W/m ² |
| Upwelling longwave radiation flux at the surface | 1.9 W/m ² | 9.4 W/m ² |

For surface temperature, comparisons with SHEBA surface observations were done by inverting measurements of the upwelling longwave flux to obtain the skin temperature. An example of the comparison is shown in Figure 7. Comparisons to three International Arctic Buoy Program (IABP) buoys located from approximately 20 km to 450 km from the SHEBA icebreaker Des Groseilliers in April–July 1998 show that the AVHRR temperatures track the buoy temperatures quite well, with mean monthly differences typically less than 2 K (not shown). Retrievals for clear sky conditions have much smaller uncertainties than for all-sky conditions, on the order of 0.3 K for the bias and 1.9 K for the RMSE [30].

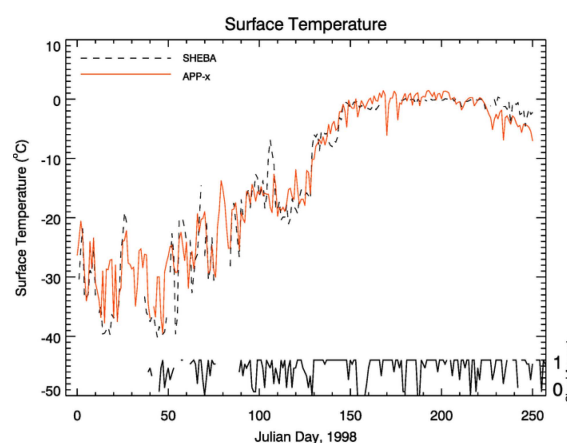


Figure 7. Comparison of satellite-derived and surface measurements of the surface skin temperature during SHEBA. Cloud amount is also shown.

Measurements of the upwelling and downwelling shortwave fluxes measured at the SHEBA camp were used to compute an all-sky albedo. Satellite-derived and surface measurements are shown in Figure 8. As with surface temperature, retrievals for clear-sky conditions have smaller uncertainties

than for all-sky conditions. The RMSE is partially caused by spatial variability at the SHEBA site. *In situ* point measurements show a local increase albedo due to snowfall for days 205–210, which increased the local surface albedo but did not carry over to the larger 25 km × 25 km area.

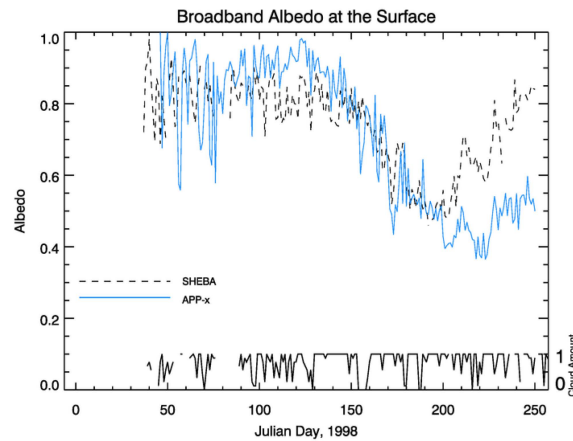


Figure 8. Comparison of satellite-derived and surface measurements of the surface broadband albedo during SHEBA. Cloud amount is also shown.

Cloud amount at the SHEBA camp is based on three-hourly synoptic observations (human observer). Comparisons with satellite-derived cloud amount for 25 × 25 km area centered on the SHEBA ship (not shown) from September 1997 through August 1998 yield a bias of 0.14 and a RMSE of 0.26.

Figure 9 gives a comparison of AVHRR-derived cloud phase and LiDAR depolarization ratio during the SHEBA year. The LiDAR results are for the highest altitude layer detected. Multilayer, multiphase cases were excluded from the analysis. The AVHRR results for a 50 × 50 km area around the LiDAR location were used, but only for scenes with a cloud fraction of at least 0.6 (60%). The AVHRR phase labeling is zero for water and one for ice; intermediate values correspond to scenes with both phases present in varying proportions. The figure illustrates that for homogeneous scenes there is almost perfect agreement between the LiDAR and satellite determinations of phase. Overall, the satellite retrievals of cloud particle phase have an accuracy of approximately 95% [28].

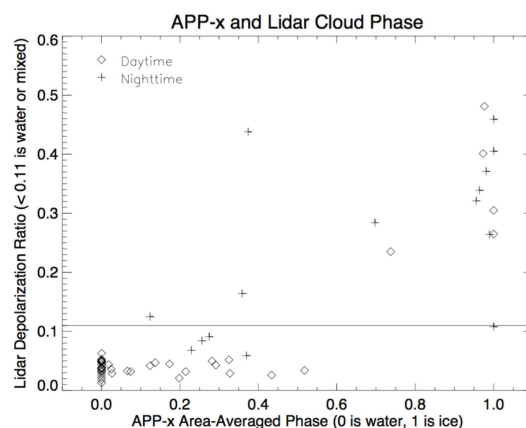


Figure 9. Cloud particle phase from the AVHRR and LiDAR depolarization ratio during the SHEBA year. Depolarization ratios less than 0.11 are primarily water or mixed-phase clouds. The AVHRR results use a value of zero for water and one for ice; intermediate values correspond to scenes with both phases present.

Cloud optical depth and particle size retrievals have not been examined in detail due to the lack of *in situ* measurements. Some comparisons have been done with aircraft observations during SHEBA, particularly with the Canadian National Research Council (NRC) Convair. The effective radius for water (liquid) clouds from the AVHRR were comparable to those measured by the Convair, typically within 1–2 μm for clouds with effective radii in the 8–10 μm range. For ice clouds the differences are larger, on the order of 10 μm for particles with effective radii in the range of 30–100 μm [31].

Cloud top pressure was validated with SHEBA LiDAR and radar measurements and TIROS Operational Vertical Sounder (TOVS) retrievals. This was a limited case study, with an uncertainty in the 50–75 hPa range.

Comparisons of instantaneous satellite-derived surface radiative fluxes with SHEBA surface measurements yield a bias of 9.8 W m^{-2} and an RMSE of 34.4 W m^{-2} for downwelling shortwave radiation. For the downwelling longwave flux, the bias and RMSE are 2.1 and 22 W m^{-2} , respectively. Figure 10 shows the results for SHEBA.

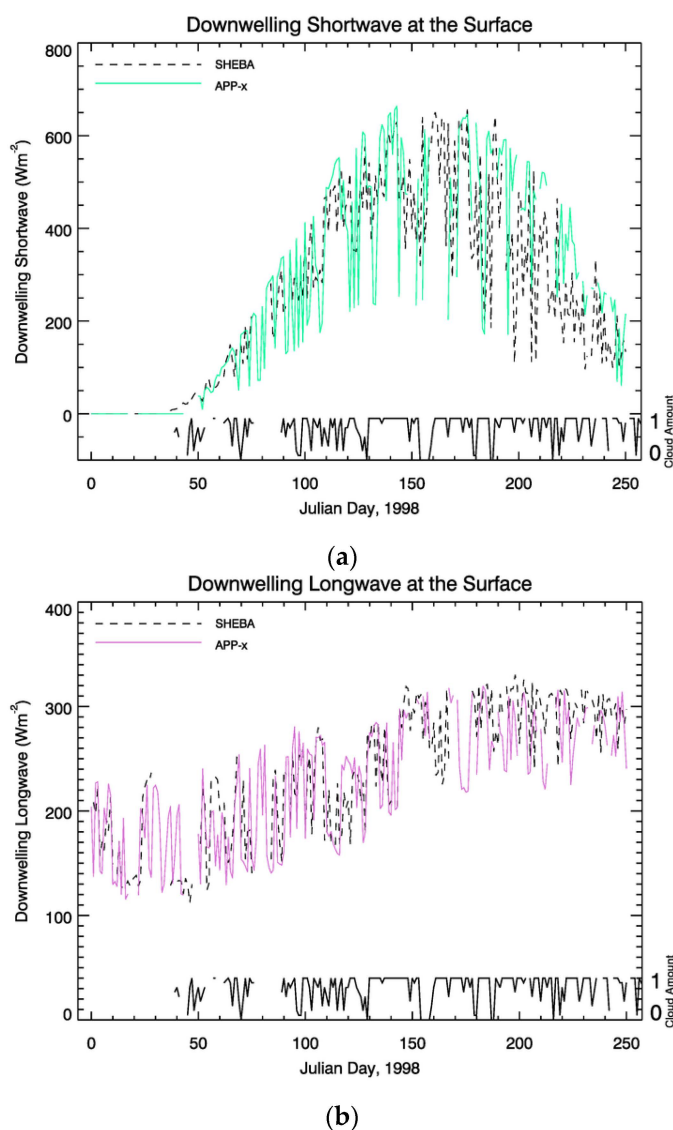


Figure 10. Comparison of satellite-derived and surface measurements of the downwelling shortwave flux at the surface (a) and the downwelling longwave flux at the surface (b). Cloud amount is also shown.

Given that the radiative fluxes in APP-x are calculated from the other retrieved variables, the theoretical combination of individual uncertainties provides some insight into the observed uncertainties in the fluxes. A theoretical approach to the propagation of errors produced uncertainties in the range of $30\text{--}50\text{ W m}^{-2}$ for the downwelling shortwave flux, $10\text{--}25\text{ W m}^{-2}$ for the downwelling longwave flux, and $30\text{--}40\text{ W m}^{-2}$ for the net flux [32]. These are similar to the SHEBA results.

4. Applications

The primary use of APP-x is for climate monitoring, trend detection, and the analysis of interactions and feedbacks in the high-latitude climate systems. This section describes a number of applications of APP-x—and indirectly APP—for climate studies. It is not meant to be an exhaustive list.

One of the first applications of APP-x led to the discovery that, over the period 1982–1999, the Arctic warmed and became cloudier in spring and summer, but cooled and became less cloudy in winter over the central Arctic Ocean, Greenland Sea, Norwegian Sea, and Barents Sea (Figure 11) [33]. The implication was that if seasonal cloud amounts did not change the way they had, surface warming would have been even greater than what was observed. The spatial and temporal variability of these and other recent changes in Arctic climate characteristics was expanded in [34] and [35]. Possible causes of the decrease in winter cloud amount were investigated in [36]. In contrast, the recent extension of APP-x through 2014 shows that the central Arctic Ocean has warmed significantly over the last 1.5 decades such that the overall effect for 1982–2014 is winter warming rather than cooling, with a weak cooling in the Siberian region (Figure 12).

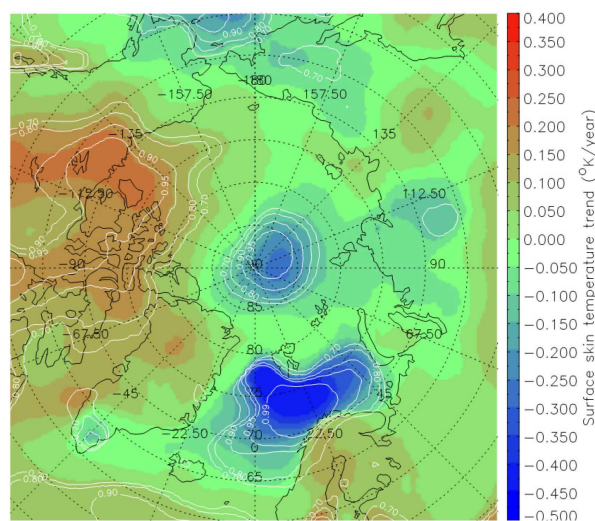


Figure 11. Surface skin temperature trend over the Arctic Ocean in winter, 1982–1999. The North Pole is at the center of the image; Greenland is in the lower left. The colors represent the trend in Kelvin per year. Contours show the statistical level of confidence of the trend. Areas with cooling trends are indicated with dashes.

The influence of trends in cloud cover and sea ice concentration on trends in Arctic Ocean surface temperature was investigated analytically and evaluated empirically with APP-x and other satellite products [37,38]. It was demonstrated that changes in ice concentration and cloud cover played major roles in the magnitude of Arctic surface temperature trends. Significant surface warming associated with sea ice loss accounted for most of the observed warming trend in autumn. In winter, cloud cover trends explain most of the surface temperature cooling. In spring, half of the warming is attributed to the trend in cloud cover.

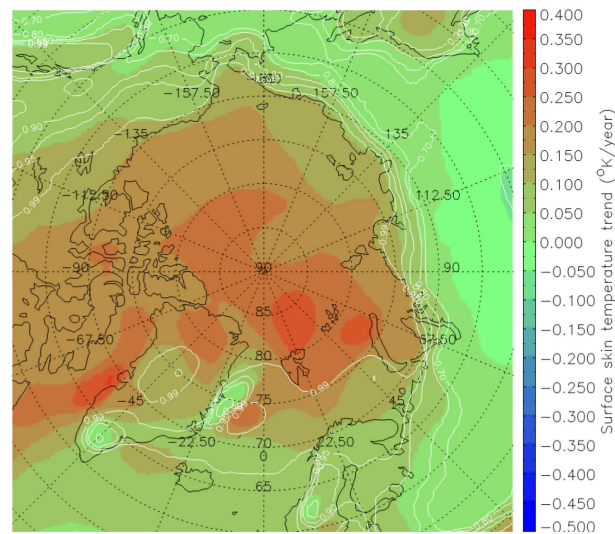


Figure 12. Same as Figure 10, but for the longer period 1982–2014.

For the south polar region, an early version of APP-x was used to discover that on a monthly time scale, clouds have a radiative warming effect on the surface of the Antarctic continent every month of the year [39]. Over the southern ocean around the continent, clouds warm the surface from April through September. This is in stark contrast to the overall cooling effect of clouds on the global scale. In a related study, cloud properties from APP-x were brought into the Arctic Regional Climate System Model (ARCSyM) to improve the simulation of the Antarctic surface energy budget. The use of APP-x resulted in improvements up to 30 W m^{-2} at the South Pole, and reduced the “spinup” time of the model [40].

Radiative fluxes from APP-x were employed to help determine the causes of variability in the Arctic minimum sea ice extent [41]. Combined with data from other satellites and atmospheric reanalyses, it was found that the downwelling longwave flux anomalies explain the most variability in the minimum ice extent, with wind anomalies being important in some areas.

As a last example, APP-x surface albedo was combined with field data to show that terrestrial changes in summer albedo contributed to recent warming trends over Alaska [42]. The lengthening of the snow-free season results in a decrease in surface albedo and an increase in local atmospheric heating on the order of several watts per square meter per decade. This is similar in magnitude to the heating expected over multiple decades due to a doubling of carbon dioxide in the atmosphere.

5. Summary and Conclusions

Rapid and large changes in Arctic and Antarctic climate over the past few decades provide the impetus for sustaining and improving the high-latitude observing systems. To fully understand not just how the climate of the polar regions is changing but also why, we need a comprehensive set of observations that includes sea ice, land cover, snow, clouds, winds, atmospheric composition, and the surface energy budget. Regional differences underscore the need for robust spatial coverage and hence the need for space-based observations.

The AVHRR Polar Pathfinder - Extended (APP-x), and the AVHRR Polar Pathfinder (APP) upon which APP-x depends, were developed to provide a number of important geophysical variables for monitoring high-latitude climates: sea ice extent and thickness, surface temperature and albedo, cloud properties, and radiative fluxes. Satellite remote sensing of the polar regions with optical (visible and infrared) sensors is notoriously difficult, particularly in the absence of sunlight, so we do not claim that the accuracy of the retrievals is any match for *in situ* measurements. Nevertheless, validation studies indicate that at least some of the products in APP-x are sufficiently accurate for trend detection, the analysis of spatial variability, and the use of anomalies in studies of interactions and feedbacks.

In particular, surface temperature, surface albedo, cloud amount, and surface radiative fluxes are considered to be of climate data record (CDR) quality.

The example applications illustrate how APP-x can be used in studies of high-latitude climate. There have been others, and there are many more possibilities. This dataset will be even more valuable as new products from other satellite instruments are developed for monitoring those characteristics of the climate system that cannot be measured by optical satellite sensors like the AVHRR. Future studies will increasingly exploit a multi-sensor approach to studying the interactions and feedbacks within the Arctic and Antarctic climate systems.

APP and APP-x will be available from the National Centers for Environmental Information (NCEI) in 2016. Future versions of APP-x will have various algorithm improvements, particularly for surface albedo, ice thickness, and cloud properties. Additionally, increases in computational power will make a 5 km version of APP-x feasible.

Acknowledgments: This work was supported by the NOAA Climate Data Records program and the National Science Foundation's Arctic System Science program (ARC 1023371). A number of people at the National Centers for Environmental Information (NCEI) Center for Weather and Climate (Asheville, North Carolina; formerly the National Climate Data Center) devoted considerable time and energy to the transition of APP and APP-x from a research environment to NCEI, notably Alisa Young, Heather Brown, and Daniel Wunder. The views, opinions, and findings contained in this report are those of the authors and should not be construed as an official National Oceanic and Atmospheric Administration or U.S. Government position, policy, or decision.

Author Contributions: Jeffrey Key originally designed and implemented APP-x and was part of the first APP project. He drafted this manuscript. Xuanji Wang modified and expanded APP-x and contributed to the APP-x and application portions of the manuscript. Yinghui Liu redesigned and implemented APP and contributed to the APP portion of the manuscript. Richard Dworak aided in APP processing and with the APP portion of the manuscript. Aaron Letterly reprocessed the validation data and contributed to the validation section of the manuscript.

Conflicts of Interest: The authors declare no conflict of interest.

References

1. IPCC. *Climate Change 2014: Impacts, Adaptation, and Vulnerability. Part. B: Regional Aspects. Contribution of Working Group II to the Fifth Assessment Report of the Intergovernmental Panel on Climate Change*; Barros, V.R., Field, C.B., Dokken, D.J., Mastrandrea, M.D., Mach, K.J., Bilir, T.E., Chatterjee, M., Ebi, K.L., Estrada, Y.O., Genova, R.C., et al, Eds.; Cambridge University Press: Cambridge, UK; New York, NY, USA, 2014.
2. Serreze, M.C.; Francis, J.A. The arctic amplification debate. *Clim. Chang.* **2006**, *76*, 241–264. [[CrossRef](#)]
3. Holland, M.M.; Bitz, C.M. Polar amplification of climate change in coupled models. *Clim. Dyn.* **2003**, *21*, 221–232. [[CrossRef](#)]
4. Kwok, R.; Untersteiner, N. The thinning of Arctic sea ice. *Phys. Today* **2011**, *64*, 36–41. [[CrossRef](#)]
5. Stroeve, J.C.; Serreze, M.C.; Holland, M.M.; Kay, J.E.; Malanik, J.; Barrett, A.P. The Arctic's rapidly shrinking sea ice cover: A research synthesis. *Clim. Chang.* **2012**, *110*, 1005–1027. [[CrossRef](#)]
6. Meier, W.; Hovelsrud, G.; van Oort, B.; Key, J.; Kovacs, K.; Michel, C.; Haas, C.; Granskog, M.; Gerland, S.; Perovich, D.; et al. Arctic sea ice in transformation: A review of recent observed changes and impacts on biology and human activity. *Rev. Geophys.* **2014**, *51*. [[CrossRef](#)]
7. Zhang, X.; Sorteberg, A.; Jing, Z.; Gerdes, R.; Comiso, J.C. Recent radical shifts of atmospheric circulations and rapid changes in Arctic climate system. *Geophys. Res. Lett.* **2008**, *35*, L22701. [[CrossRef](#)]
8. Wu, Q.; Zhang, J.; Zhang, X.; Tao, W. Interannual variability and long-term changes of atmospheric circulation over the Chukchi and Beaufort Seas. *J. Clim.* **2014**, *27*, 4871–4889. [[CrossRef](#)]
9. Walsh, J.E.; Kattsov, V.M.; Chapman, W.L.; Govorkova, V.; Pavlova, T. Comparison of arctic climate simulations by uncoupled and coupled global models. *J. Clim.* **2002**, *15*, 1429–1446. [[CrossRef](#)]
10. Francis, J.A.; White, D.M.; Cassano, J.J.; Gutowski, W.J., Jr.; Hinzman, L.D.; Holland, M.M.; Steele, M.A.; Voeroesmarty, C.J. An arctic hydrologic system in transition: Feedbacks and impacts on terrestrial, marine, and human life. *J. Geophys. Res. Biogeosci.* **2009**, *114*. [[CrossRef](#)]
11. Turner, J.; Colwell, S.R.; Marshall, G.J.; Lachlan-Cope, T.A.; Carleton, A.M.; Jones, P.D.; Lagun, V.; Reid, P.A.; Iagovkina, S. Antarctic climate change during the last 50 years. *Int. J. Climatol.* **2005**, *25*, 279–294. [[CrossRef](#)]

12. Zwally, H.J.; Li, J.; Robbins, J.W.; Saba, J.L.; Yi, D.; Brenner, A.C. Mass gains of the Antarctic ice sheet exceed losses. *J. Glaciol.* **2015**. [[CrossRef](#)]
13. Meier, W.; Maslanik, J.; Key, J. Multiparameter AVHRR-derived products for Arctic climate studies. *Earth Interact.* **1997**, *1*, 1–29. [[CrossRef](#)]
14. Liu, Y.; Key, J.; Heidinger, A. *Climate Algorithm Theoretical Basis Document, AVHRR Polar Pathfinder (APP)*; CDRP-ATBD-0572, Revision 1.0; NOAA/NESDIS Center for Satellite Applications and Research and The National Centers for Environmental Information: Asheville, NC, USA, 2015.
15. Key, J.; Wang, X. *Climate Algorithm Theoretical Basis Document, Extended AVHRR Polar Pathfinder (APP-x)*; CDRP-ATBD-0573, Revision 1.0; NOAA/NESDIS Center for Satellite Applications and Research and The National Centers for Environmental Information: Asheville, NC, USA, 2015.
16. Kidwell, K.B. *NOAA KLM User's Guide with NOAA-N, -P Supplement (February 2009 Revisions)*; NOAA/NESDIS: Washington, DC, USA, 2009.
17. Nolin, A.W.; Armstrong, R.; Maslanik, J. *Near-Real-Time SSM/I-SSMIS EASE-Grid Daily Global Ice Concentration and Snow Extent, Version 4*; NASA National Snow and Ice Data Center Distributed Active Archive Center: Boulder, CO, USA, 1998.
18. NOAA/STAR. Available online: http://www.star.nesdis.noaa.gov/smcd/emb/vci/VH/vh_avhrr_ect.php (accessed on 22 February 2016).
19. Heidinger, A.K.; Straka, W.C., III; Molling, C.C.; Sullivan, J.T.; Wu, X. Deriving an inter-sensor consistent calibration for the AVHRR solar reflectance data record. *Int. J. Remote Sens.* **2010**, *31*, 6493–6517. [[CrossRef](#)]
20. Molling, C.C.; Heidinger, A.K.; Straka, W.C., III; Wu, X. Calibrations for AVHRR channels 1 and 2: Review and path towards consensus. *Int. J. Remote Sens.* **2010**, *31*, 6519–6540. [[CrossRef](#)]
21. Rienecker, M.M. MERRA: NASA's Modern-era retrospective analysis for research and applications. *J. Clim.* **2011**, *24*, 3624–3648. [[CrossRef](#)]
22. Key, J.R.; Collins, J.B.; Fowler, C.; Stone, R.S. High-latitude surface temperature estimates from thermal satellite data. *Remote Sens. Environ.* **1997**, *61*, 302–309. [[CrossRef](#)]
23. Key, J.; Haeffliger, M. Arctic ice surface-temperature retrieval from avhrr thermal channels. *J. Geophys. Res.-Atmos.* **1992**, *97*, 5885–5893. [[CrossRef](#)]
24. Key, J.; Wang, X.; Stroeve, J.; Fowler, C. Estimating the cloudy sky albedo of sea ice and snow from space. *J. Geophys. Res.* **2001**, *106*, 12489–12497. [[CrossRef](#)]
25. Wang, X.; Key, J.; Liu, Y. A thermodynamic model for estimating sea and lake ice thickness with optical satellite data. *J. Geophys. Res.* **2010**, *115*, C12035. [[CrossRef](#)]
26. Key, J.; Schweiger, A.J. Tools for atmospheric radiative transfer: Streamer and FluxNet. *Comput. Geosci.* **1998**, *24*, 443–451. [[CrossRef](#)]
27. Key, J.; Barry, R.G. Cloud cover analysis with Arctic AVHRR, part 1: Cloud detection. *J. Geophys. Res.* **1989**, *94*, 18521–18535. [[CrossRef](#)]
28. Key, J.; Intrieri, J. Cloud particle phase determination with the AVHRR. *J. Appl. Meteorol.* **2000**, *39*, 1797–1805. [[CrossRef](#)]
29. Nakajima, T.; King, M.S. Determination of the optical thickness and effective particle radius of clouds from reflected solar radiation measurements. Part I: Theory. *J. Atmos. Sci.* **1990**, *47*, 1878–1893. [[CrossRef](#)]
30. Key, J.; Maslanik, J.A.; Papakyriakou, T.; Serreze, M.C.; Schweiger, A.J. On the validation of satellite-derived sea ice surface temperature. *Arctic* **1994**, *47*, 280–287. [[CrossRef](#)]
31. Gultepe, I.; Isaac, G.; Key, J.; Uttal, T.; Intrieri, J.; Starr, D.; Strawbridge, K. Dynamical and microphysical characteristics of arctic clouds using integrated observations collected over sheba during the April 1998 FIRE-ACE flights of the Canadian Convair, Meteorol. Atmos. Phys. **2004**, *85*, 235–263. [[CrossRef](#)]
32. Key, J.; Schweiger, A.J.; Stone, R.S. Expected uncertainty in satellite-derived estimates of the high-latitude surface radiation budget. *J. Geophys. Res.* **1997**, *102*, 15837–15847. [[CrossRef](#)]
33. Wang, X.J.; Key, J.R. Recent trends in arctic surface, cloud, and radiation properties from space. *Science* **2003**, *299*, 1725–1728. [[CrossRef](#)] [[PubMed](#)]
34. Wang, X.J.; Key, J.R. Arctic surface, cloud, and radiation properties based on the AVHRR polar pathfinder dataset. Part I: Spatial and temporal characteristics. *J. Clim.* **2005**, *18*, 2558–2574.
35. Wang, X.J.; Key, J.R. Arctic surface, cloud, and radiation properties based on the AVHRR polar pathfinder dataset. Part II: Recent trends. *J. Clim.* **2005**, *18*, 2575–2593.

36. Liu, Y.; Key, J.; Francis, J.; Wang, X. Possible causes of decreasing cloud cover in the Arctic winter, 1982–2000. *Geophys. Res. Lett.* **2007**, *34*, L14705. [[CrossRef](#)]
37. Liu, Y.; Key, J.; Wang, X. Influence of changes in sea ice concentration and cloud cover on recent arctic surface temperature trends. *Geophys. Res. Lett.* **2009**, *36*. [[CrossRef](#)]
38. Liu, Y.; Key, J.; Wang, X. The influence of changes in cloud cover on recent surface temperature trends in the arctic. *J. Clim.* **2008**, *21*, 705–715. [[CrossRef](#)]
39. Pavolonis, M.; Key, J. Antarctic cloud radiative forcing at the surface data sets, 1985–1993. *J. Appl. Meteorol.* **2003**, *42*, 827–840. [[CrossRef](#)]
40. Pavolonis, M.; Key, J.; Cassano, J. A study of the Antarctic surface energy budget using a coupled regional climate model forced with satellite-derived cloud properties. *Mon. Wea. Rev.* **2004**, *132*, 654–661. [[CrossRef](#)]
41. Francis, J.A.; Hunter, E.; Key, J.; Wang, X. Clues to variability in Arctic minimum sea ice extent. *Geophys. Res. Lett.* **2005**, *32*, L21501. [[CrossRef](#)]
42. Chapin, F.S.; Sturm, M.; Serreze, M.C.; McFadden, J.P.; Key, J.R.; Lloyd, A.H.; McGuire, A.D.; Rupp, T.S.; Lynch, A.H.; Schimel, J.P.; *et al.* Role of land surface changes in Arctic summer warming. *Science* **2005**, *310*. [[CrossRef](#)] [[PubMed](#)]



© 2016 by the authors; licensee MDPI, Basel, Switzerland. This article is an open access article distributed under the terms and conditions of the Creative Commons by Attribution (CC-BY) license (<http://creativecommons.org/licenses/by/4.0/>).